

Modeling and Fabrication of Silk Fibroin–Gelatin-Based Constructs Using Extrusion-Based Three-Dimensional Bioprinting

Diego Trucco, Aarushi Sharma, Cristina Manferdini, Elena Gabusi, Mauro Petretta, Giovanna Desando, Leonardo Ricotti, Juhi Chakraborty, Sourabh Ghosh,* and Gina Lisignoli*

Cite This: *ACS Biomater. Sci. Eng.* 2021, 7, 3306–3320

Read Online

ACCESS |

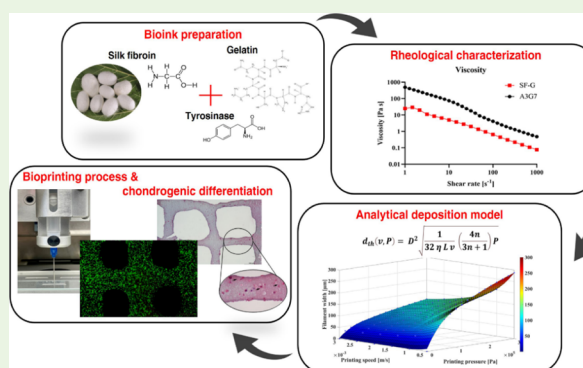
Metrics & More

Article Recommendations

Supporting Information

ABSTRACT: Robotic dispensing-based 3D bioprinting represents one of the most powerful technologies to develop hydrogel-based 3D constructs with enormous potential in the field of regenerative medicine. The optimization of hydrogel printing parameters, proper geometry and internal architecture of the constructs, and good cell viability during the bioprinting process are the essential requirements. In this paper, an analytical model based on the hydrogel rheological properties was developed to predict the extruded filament width in order to maximize the printed structure's fidelity to the design. Viscosity data of two natural hydrogels were imputed to a power-law model to extrapolate the filament width. Further, the model data were validated by monitoring the obtained filament width as the output. Shear stress values occurring during the bioprinting process were also estimated. Human mesenchymal stromal cells (hMSCs) were encapsulated in the silk fibroin–gelatin (G)-based hydrogel, and a 3D bioprinting process was performed to produce cell-laden constructs. Live and dead assay allowed estimating the impact of needle shear stress on cell viability after the bioprinting process. Finally, we tested the potential of hMSCs to undergo chondrogenic differentiation by evaluating the cartilaginous extracellular matrix production through immunohistochemical analyses. Overall, the use of the proposed analytical model enables defining the optimal printing parameters to maximize the fabricated constructs' fidelity to design parameters before the process execution, enabling to achieve more controlled and standardized products than classical trial-and-error approaches in the biofabrication of engineered constructs. Employing modeling systems exploiting the rheological properties of the hydrogels might be a valid tool in the future for guaranteeing high cell viability and for optimizing tissue engineering approaches in regenerative medicine applications.

KEYWORDS: 3D bioprinting, cartilage tissue engineering, analytical deposition model, silk fibroin, hydrogel, human mesenchymal stromal cells



1. INTRODUCTION

Extrusion-based 3D bioprinting provides a strategy to deposit alive cells in a defined position to prepare neo-engineered tissue constructs to foster the regeneration of target tissues.^{1–5} In this strategy, precisely controlled extrusion of a hydrogel provides a 3D structure design in which cells can be homogeneously embedded and distributed in a spatially controlled manner throughout the volume of the printed construct, to allow an efficient diffusion of nutrients and permit the cells to undergo self-assembly.^{6–8} The properties of the bioprinted construct depend on the hydrogel materials,^{9–11} strategies to induce sol-to-gel transition, and the fabrication process (printing parameters).¹² Different natural biopolymers (i.e., alginate (A), methylcellulose, agarose, gelatin (G), collagen, gellan gum, hyaluronic acid, and silk fibroin (SF)) are used in regenerative medicine.^{13–15} These natural polymer hydrogels are biodegradable, allow diffusion of nutrients, and support cellular differentiation processes. The fabrication

process must be performed following precisely controlled parameters (i.e., accurate prediction of filament deposition), ensuring the fidelity of the fabricated constructs to the designed internal architectures, mechanical compliance, cell viability, and the promotion of new tissue formation.^{2,16}

Nowadays, efforts in the 3D bioprinting field are mainly driven by experiments and trial-and-error approaches.¹⁷ Various factors affect the printing process, such as the printing pressure speed and temperature, needle length and inner diameter, as well as characteristics of the hydrogel (sol-to-gel transition time, viscosity, temperature, and rheological

Received: March 25, 2021

Accepted: May 18, 2021

Published: June 8, 2021



characteristics).⁵ Gelation strategies also play a crucial role in controlling printability, such as covalent bond formation through ultraviolet irradiation, enzymatic cross-linking, or noncovalent bond formation through hydrogen bonds using ionic interactions.^{15,18,19} Appropriate models would allow to save time and resources and have more predictable and reliable results, allowing higher repeatability and standardization of the process,²⁰ as well as preprocess evaluation of shear stresses applied to the cells. Few studies in the state of the art focused on analytical and/or computational models to understand and plan bioprinting processes. For example, Paxton *et al.*²¹ developed an approach to estimate the printing window of different materials, including Pluronic and alginate-based formulations, considering printing parameters such as pressure and speed. Computational fluid dynamics (CFD) simulations concerning pressure drop over the printing head and maximal shear parameters at the outlet were proposed by Emmermacher *et al.*²² to optimize the process, focusing on material properties, flow parameters, and needle diameter. Zhao *et al.*²³ presented a systematic investigation on the influence of 3D cell printing parameters, evidencing that the cell survival rate increased with the bioink viscoelasticity. Finally, Suntonmond *et al.*²⁴ proposed a model to predict the printed width of a continuous synthetic hydrogel line in which the resolution was expressed as a function of nozzle size, printing pressure, and speed.

Generally, bioprinting models were developed based on the rheological properties of fully synthetic bioinks (*i.e.*, Nivea cream²¹ and Pluronic^{21,24}), but no models have been proposed and validated so far for natural polymer-blended bioinks. Among the natural polymers used for tissue regeneration, SF–G-based hydrogels have emerged as promising biomaterials for cartilage^{25,26} and bone regeneration²⁷ thanks to their chemical and biological properties. Interestingly, silk fiber produced by the silkworm consists of two-component proteins, namely, fibroin (70–80%) and sericin (20–30%).²⁸ Fibroin exists in three distinct structural conformations: silk I, silk II, and silk III.²⁸ The sericin protein may create an immunological response, so it must be removed.²⁹ A degumming process can be performed to remove sericin proteins and to obtain a pure SF solution.³⁰ Three-dimensional printing of only silk protein is highly challenging. The first report of 3D printing of only SF solution was done using advanced direct-write techniques,³¹ which required the exposure of silk solution in an alcohol coagulation bath. Regenerated silk solution is formed by the dissolution of the silk cocoons. During the processing of silk cocoons to silk solution, silk chains are fragmented into small sizes,³² causing the reduction in the overall molecular weight. This fragmentation is reported to drastically affect the rheological aspects of the silk chains. In comparison, native silk solution of 24% concentration displayed a high shear viscosity of 1722 Pa·s,³³ which dropped to about 0.5 Pa·s for regenerated SF.³⁴ This vast change in viscosity of the silk solution, in both native and regenerated solutions, might be due to the denaturation of the silk chains during degumming and dissolution of the silk cocoons. This drop in the viscosity was being recovered by blending silk solutions with high-viscosity fluids, such as gelatin, gel-MA,³⁵ and so forth. Native SF produced by the silkworm show shear-induced gelation. However, for bioprinting using regenerated silk solution, a cross-linking mechanism needs to be devised for the fabrication of stable constructs. The addition of gelatin with SF protein allowed the development of a printable bioink,

as the elastic modulus of the blend was improved.³⁴ A number of reasons are responsible: first, the SF–G blend facilitated interchain interactions due to the hydrophobic interactions between the two protein macromolecules.³⁶ Differences in the isoelectric point of silk and gelatin could lead to the formation of the physical gel. The isoelectric point of silk is lower than 7, while that of gelatin is greater than 7. Under physiological conditions (pH 7.2–7.4), opposite charges of these two biomacromolecules develop electrostatic interactions.³⁴ However, the printability window for this SF–G-blended bioink composition needs to be carefully optimized.

Achieving an agreement between proper shape and porosity of the cell-laden matrix and the overall stability of the construct are still challenges in the field of 3D bioprinting. This also concerns gelatin-based hydrogels, for which no model has been developed so far, which is essential to optimize their printing and to predict the best fabrication parameters needed to achieve porous and stable structures matching the design parameters, thus permitting good nutrient diffusion and high cell viability. The analytical models can be useful to achieve more controlled and standardized conditions than classical approaches for designing clinically useful engineered constructs. Indeed, preliminary studies have to focus on selecting the ink owing to the best physicochemical conditions to ensure both good printability and biological responses. Scaffold features like the fiber diameter need to be considered as they are crucial environmental cues that strongly influence the cell behavior.³⁷ Our study mainly addressed modeling natural bioinks which better recapitulate biological mechanisms implicated in tissue repair. We focused on SF because of its promising results in osteochondral repair. In this study, the optimal printing parameters set to achieve optimal fidelity of the fabricated constructs with respect to the design parameters were identified for two gelatin-based hydrogels, starting from the evaluation of material rheological properties. An analytical model to predict the deposited filament width using the extrusion-based 3D bioprinting system was implemented and validated.²⁴ Variations in the key printing parameters, such as pressure and speed, were evaluated by using different combinations of needle lengths and inner diameters for an experimental validation of the model. Additionally, the shear stress occurring during SF–G bioprinting was predicted to ensure subsequent cell viability during the printing process. Viability was evaluated on embedded human mesenchymal stromal cells (hMSCs) in SF–G-based bioinks. Finally, cartilaginous extracellular matrix (ECM) production was assessed through immunohistochemical analysis.

2. MATERIALS AND METHODS

2.1. Materials. The *Bombyx mori* cocoons were provided by Central Silk Technological Research Institute (Central Silk Board, Bangalore, Ministry of Textiles, Government of India). Lithium bromide (LiBr, Merck), sodium carbonate (Na₂CO₃, Merck), and dialysis cassette (Merck) were purchased to extract the SF solution. Gelatin powder from porcine skin type A (Merck), mushroom tyrosinase enzyme (Merck), and sodium alginate (Merck) were used to form hydrogels. Calcium chloride (CaCl₂, Merck) was used to carry out ionic cross-linking. Cell expansion and culture were performed using Dulbecco's modified Eagle's medium (DMEM) high-glucose medium (EuroClone), fetal bovine serum (FBS) (EuroClone), penicillin/streptomycin (Gibco), and trypsin/EDTA (EuroClone).

2.2. SF Extraction. A SF-based solution from *B. mori* cocoons was obtained following a previously published extraction protocol.³⁰

Briefly, 2.5 g of cocoons was cut with scissors and boiled twice in 0.02 M Na₂CO₃ for 20 min and then washed in distilled water to remove sericin. The fibers were dried at 37 °C overnight and then dissolved in 9.3 M LiBr solution for 4 h at 60 °C. After cooling at room temperature (RT), the SF solution was dialyzed using a dialysis cassette (12–14 kDa cutoff) against deionized water at RT. Water was changed six times during the first day and three times during the second day (total dialysis time: 48 h). Then, the SF solution was stored at 4 °C. Finally, the protein percentage determination of the SF solution was performed as previously described.^{30,38}

2.3. Bioink Preparation. G (5% w/v, 75 mg) and SF solution (5% w/v, 1.2 mL) were blended and then mixed to obtain a final volume (1.5 mL) of the bioink. To achieve a limpid solution, the blended materials were incubated in a thermostatic bath at 37 °C for 30 min. DMEM (10X, 150 μL) and 10% FBS (150 μL) were added to the SF–G solution. Finally, the mushroom tyrosinase enzyme (430 U/1.5 mL) was added to the bioink, as previously reported.³⁸

G (3% w/v) and A (7% w/v) powders were dissolved under constant magnetic agitation at 60 °C for 1 h and at RT for the other 2 h.³⁹ The A3G7 blend was heated at 37 °C for 45 min and then transferred in syringes to be stored at 4 °C until they were used. Before printing it, the syringe was heated at 37 °C for 1 h, and the bioink was transferred to a new cartridge. The cartridge was left for 2 h at RT to reach 25 °C before starting the printing. Finally, 1 mL of CaCl₂ solution (1% w/v) was added on top of the printed construct to cover it completely and to perform ionic cross-linking. After 5 min, the solution was removed.

2.4. Rheological Characterization. The rheological properties of the blends were measured by a rheometer (Anton Paar MCR-302) with a plate–plate geometry, using a plate with 25 mm diameter and a gap of 1 mm. The viscosity of SF–G was measured 20 min after the addition of the mushroom tyrosinase enzyme at 21 °C, whereas the viscosity of A3G7 was measured at 25 °C for shear rates ranging from 0.1 to 1000 s⁻¹ in rate-controlled modality. The flow behavior was further evaluated in the linear region by plotting viscosity against the shear rate in a log–log scale graph.

2.5. Analytical Model for Filament Width Prediction. To understand the influence of the printing parameters such as pressure and printing speed on the width of the deposited filament at different needle sizes, an analytical model of deposition was developed. The rheological characterizations evidenced that, as the applied shear stress was increased, the viscosities decreased; so, both fluids showed a pseudoplastic behavior. We assumed the flow to be a Hagen–Poiseuille flow, with a non-Newtonian viscosity (shear thinning), to be modeled with a power-law function.⁴⁰ In this case, when the reference shear rate ($\dot{\gamma}_0$) has unit value, we can express the relationship between viscosity and shear rate as follows

$$\eta = K\dot{\gamma}^{n-1} \quad (1)$$

where η is the apparent viscosity, K is the consistency index (initial viscosity), $\dot{\gamma}$ is the shear rate, and n is the power-law index.

The model was based on the relationship between stress and shear rate, assuming that the extrusion-based 3D bioprinting strategy is similar to that of a capillary rheometer,²⁴ namely

$$\tau_w = \eta\dot{\gamma}_w \quad (2)$$

where τ_w is the maximum stress. In a capillary, in the presence of laminar flow, this can be expressed as

$$\tau_w = \frac{RP}{2L} \quad (3)$$

where R and L are the radius and length, respectively, of the extrusion nozzle, while P represents the printing pressure. The shear rate, which depends on the volumetric flow rate (Q), can be expressed as

$$\dot{\gamma}_w = \left(\frac{3n+1}{4n}\right)\left(\frac{4Q}{\pi R^3}\right) \quad (4)$$

The volumetric flow rate, under the assumptions of constant strand geometry during the deposition process, is expressed by

$$Q = \frac{\pi d^2}{4} \nu \quad (5)$$

where d is the strand diameter, and ν is the printing speed. By substituting eqs 3–5 to eq 2, the following relationship (6) can be obtained, which links d to the pressure applied (P), the printing speed (ν), the nozzle diameter (D), and other parameters

$$d_{th}(\nu, P) = D^2 \sqrt{\frac{1}{32\eta L \nu} \left(\frac{4n}{3n+1}\right) P} \quad (6)$$

This model was used to predict the achieved fiber diameter as a function of the key parameters used in the fabrication process. To validate this, different parameter values were set. In particular, P was varied from 0 to 3×10^5 Pa for the SF–G bioink and from 0 to 4×10^5 Pa for the A3G7 bioink with 0.2×10^5 Pa steps; ν was varied from 0.5 to 3×10^{-3} m/s for the SF–G bioink and from 0.5 to 6×10^{-3} m/s for the A3G7 bioink with 0.5×10^{-3} m/s steps; D was evaluated at 0.05, 0.2, 0.41, 0.5, and 1 mm; and L was tested for 6.35, 12.7, and 25.4 mm needles. The different needle types are summarized in Table 1.

Table 1. Characteristics of the Different Needle Types Considered in This Study

needle ID	diameter (D) [mm]	length (L) [mm]	verified through experiments
D0.05_L6.35	0.05	6.35	no
D0.05_L12.7	0.05	12.7	no
D0.05_L25.4	0.05	25.4	no
D0.20_L6.35	0.20	6.35	yes
D0.20_L12.7	0.20	12.7	yes
D0.20_L25.4	0.20	25.4	yes
D0.41_L6.35	0.41	6.35	yes
D0.41_L12.7	0.41	12.7	yes
D0.41_L25.4	0.41	25.4	yes
D0.50_L6.35	0.50	6.35	yes
D0.50_L12.7	0.50	12.7	yes
D0.50_L25.4	0.50	25.4	yes
D1.00_L6.35	1.00	6.35	no
D1.00_L12.7	1.00	12.7	no
D1.00_L25.4	1.00	25.4	no

2.6. Experimental Validation of the Model. **2.6.1. Bioink Filament Printing and Imaging.** Experimental tests with the SF–G and A3G7 bioinks were performed to assess the width of the filaments by varying the different parameters, thus, to validate the model. We designed the desired pattern through the software BioCAD (RegenHU, Villaz-St-Pierre, CH) that was subsequently converted into a G-code and deposited through a 3D Discovery platform (RegenHU) utilizing a direct dispenser printhead, using stainless steel cylindrical shaped needles for all the tests. The needles were chosen for experimental tests with lengths of 6.35, 12.7, and 25.4 mm, and for each length, the following diameters were tested: 0.2, 0.41, and 0.5 mm, for a total of nine different needles (Table 1). The design consisted of a layered square with an internal pattern composed of two parallel lines at relative angles of 0 and 90° with an interfilament distance of 1 mm in both directions (x and y). Each pattern was printed three times using the needles previously described in all combinations of both P and ν used in the analytical model. At the beginning of the process, the distance between the printing needle tip and the printing bed surface was set as 2/3 of the needle diameter; thus, for the needles having diameters of 0.20, 0.41, and 0.50 mm, we set distances of 0.13, 0.27, and 0.33 mm, respectively, following a criterion previously reported in the literature.²¹ Moreover, the layer height chosen for each needle was equal to 80% of the inner diameter to ensure proper layer adhesion. The bioprinter internal temperature was kept at 21 ± 1 °C during the printing process of SF–G and $25 \pm$

1 °C during the printing process of A3G7. The printing bed surface was always kept at RT without allowing any cooling or heating of the surface. An image of each printed pattern was captured through an optical microscope (Nikon Eclipse 90i, DS-Ri2, Nikon Instruments Europe BV, Tokyo, Japan). The width of the deposited filaments was measured using a dedicated image processing software (NIS-Elements, Nikon Instruments Europe BV, Tokyo, Japan). The extruded filament width was measured, considering the filament included between two filaments' cross-points. Images ($N > 20$) were captured, and the width values were compared with the ones predicted by the model. Data were expressed as average value \pm standard deviation (average value \pm SD).

2.6.2. Model Validation. To validate the analytical model with the experimentally acquired data, we calculated the percentage error for each condition tested. Such an error was calculated as follows

$$\%_{\text{err}} = 100 \times \frac{d - d_{\text{exp}}}{d_{\text{exp}}} \quad (7)$$

where d was the filament width predicted by the model and d_{exp} was the experimental result obtained. The error percentage gave indications on the ability of the model to correctly predict the output. Moreover, it also allowed evaluation of the filament width to determine whether it was underestimated or overestimated by the model for the different printing parameters and needle features. In the state of the art, no specific cutoff values for the error are indicated as acceptable ones. In our case, we identified 20% as an acceptable error cutoff. This choice was related to the specific case selected for our proof of concept (filament width = $238 \pm 26 \mu\text{m}$). We considered it acceptable to have a possible real filament width of $246 \mu\text{m}$ (corresponding to a 20% error); as this variation would have no crucial implications on cell viability, the designed 3D structure would keep a relatively high porosity value, also in the worst case.

2.6.3. Shear Stress Estimation. During the bioprinting procedure, cells are subjected to inevitable shear stress. To guarantee good cell viability, such shear stress should be minimized.⁴¹

To calculate the maximum shear stress values applied during the printing of the SF-G bioink, the volumetric flow rate (Q) was first quantified. Several SF-G bioink dispensing tasks were conducted to quantify Q at varying pressures and needle sizes and lengths. An integrated camera (DinoCamera, Dino-Lite Europe, The Netherlands) included in the 3D Discovery platform was positioned perpendicularly to the needles to capture the extruded filaments, as shown in Figure S1.

For each video, a fixed distance was defined, drawing a line (red line in Figure S1), and it was established by camera calibration defining the magnification length, considering it as a known distance from the nominal outer diameter of the needle. The magnification was equal to a fixed distance of 11.86 mm. Several videos (three for each pressure value) were captured at four different pressures (1, 1.5, 2, and 2.5×10^5 Pa) during the extrusion procedure for all needles with a diameter of 0.2 mm. The average time employed by the filaments to cover the fixed distance (from the top to the bottom of the red line) was measured and was then used to extrapolate the velocities of filament extrusion for each needle at different pressures used. The corresponding volumetric flow rates (Q) were calculated through eq 5. Under the first assumption, namely that the flow is a Hagen-Poiseuille one, with a non-Newtonian viscosity modeled with a power-law function, the analytical equation of the bioink velocity is expressed by (8)

$$v(r) = \frac{n}{n+1} \left(\frac{P}{2LK} \right)^{1/n} (R^{n+1/n} - r^{n+1/n}) \quad (8)$$

To compute the maximum shear stress using eq 2, P can be extrapolated by computing the volume flow rate Q by averaging the velocity solution

$$Q = \bar{v}A \int_A v(r) \pi R^2 dr = \left(\frac{-P}{2LK} \right)^{1/n} \left(\frac{n}{3n+1} \right) R^{n+1/n} \pi R^2 \quad (9)$$

From (9), we obtained the expression of P as follows

$$P = -2KL \left[Q \left(\frac{3n+1}{n} \right) R^{-3n+1/n} \right]^n \quad (10)$$

Finally, in the case of capillary and laminar flows of non-Newtonian fluids, the maximum shear stress was estimated using eq 2, which can also be expressed as (11)

$$\tau_w = \frac{RP}{2L} = -KR \left[Q \left(\frac{3n+1}{n} \right) R^{-3n+1/n} \right]^n \quad (11)$$

The velocities and consequently the volumetric flow rate Q were fitted with the corresponding four average pressures using exponential fitting (a power law).^{40,42} These fitting curves were then used to extrapolate the Q values for each needle at the pressure value used in the analytical model (from 0 to 3×10^5 Pa with 0.2×10^5 Pa steps). The shear stress values were thus calculated from eq 11 for all pressure values ($0-3 \times 10^5$ Pa) and needle types.

2.7. Cell Encapsulation and Bioprinting Process. **2.7.1. Printing Parameters.** The construct design consisted of a layered square with dimensions of 6×6 mm (length \times width). After the model validation, the bioprinting process to deposit the SF-G bioink with encapsulating cells was carried out using only a D0.20_L6.35 needle to guarantee satisfactory nutrients and factors to cells, thanks to a high structure porosity. The porosity indicates the amount of void space within a structure, while permeability is a measure of how easily a fluid can flow through the structure.⁴³ Additionally, the nutrients' diffusion through the printed filament can be improved by using the smallest tested needle to print a tight filament.⁴⁴ Finally, the shear stress to cells was minimized using the shortest needle length tested. The final 3D structures were printed using P of 1.2×10^5 Pa and v of 1.5×10^{-3} m/s, extracted by the analytical model. The 3D constructs were composed of 10 layers, featuring an overall thickness of 1.2 mm.

2.7.2. Cell Encapsulation and Bioprinting. Bone marrow was harvested from an anonymous healthy donor to isolate hMSCs, as previously reported.⁴⁵ 1×10^7 hMSCs at passage 3 were encapsulated into 1.5 mL of SF-G-based bioink, immediately after the addition of 430 U of tyrosinase (Sigma-Aldrich) under a laminar flow at RT, and biological triplicates were carried out. hMSC-laden SF-G bioinks were gently loaded into sterile cartridges and closed by sterile pistons and needles.³⁸ The cartridge was then mounted on the pressure-based direct dispensing printhead of the 3D Discovery Bioprinting platform (RegenHU). The bioprinting process was started 20 min after enzyme addition to allow a suitable initial degree of gelation, maintaining the temperature at 21 ± 1 °C. Twelve constructs were printed with the above-mentioned internal microarchitecture and 10 layers of thickness, using the printing parameters previously specified. The extruded filament width was measured at the level of the filaments between two filaments' cross-point by capturing images and comparing to the one predicted by the model. Data were expressed as average value \pm standard deviation (average value \pm SD).

2.7.3. Cell Viability. The cell viability of hMSC-laden 3D SF-G constructs was determined immediately after the bioprinting process and 28 days later by the live and dead cell viability assay (Thermo Fisher Scientific, USA). The constructs were washed with phosphate-buffered saline (PBS) and then incubated with ethidium homodimer-1 (4 μM) and calcein-AM (2 μM) for 45 min at 37 °C. After two washing steps with PBS, the constructs were evaluated by a microscope (Eclipse 90i microscope, Nikon, Japan) using fluorescein isothiocyanate and TRITC filters to assess viable (green) and dead/necrotic (red) cells.

2.7.4. Chondrogenic Differentiation and Immunohistochemical Analysis. hMSC-laden 3D SF-G constructs were cultured both in the control chondrogenic medium—DMEM high-glucose supplemented with ITS (6.25 $\mu\text{g}/\text{mL}$ of insulin, 6.25 $\mu\text{g}/\text{mL}$ of transferrin, and 6.25 $\mu\text{g}/\text{mL}$ of di-selenium) (Sigma-Aldrich), premix (5.33 $\mu\text{g}/\text{mL}$ of linoleic acid and 1.25 mg of bovine serum albumin), 0.1 μM dexamethasone (Sigma-Aldrich), 37.5 $\mu\text{g}/\text{mL}$ ascorbic acid (Sigma-Aldrich), 1 mM sodium pyruvate (Sigma-Aldrich), 100 U/mL penicillin (Sigma-Aldrich), and 100 $\mu\text{g}/\text{mL}$ streptomycin (Sigma-

Aldrich) and in the chondrogenic differentiation medium (control chondrogenic medium containing 10 ng/mL TGF- β 3). After 28 days, the constructs were embedded in the optimal cutting temperature compound (Kalttek srl, Padova, Italy) before being snap-frozen in liquid nitrogen. Sections (thickness—12 μ m) were cut, air-dried, and stored at -20 $^{\circ}$ C until they were used. Briefly, the slides were fixed in 10% formaldehyde (Kalttek, Italy) for 1 h, rehydrated with Trisbuffered saline, and the nonspecific antigenic sites were blocked with Protein Block Serum-Free (Dako, Glostrup, Denmark) for 10 min at RT. Sections were incubated with monoclonal mouse antihuman collagen type 2 (diluted 1:20) and anti-SOX-9 (diluted 1:50) antibodies (all from Chemicon International, Temecula, CA, USA) for 1 h at RT. Later, the samples were rinsed and incubated with multilinked biotinylated secondary antibody and alkaline phosphatase-conjugated streptavidin (Biocare Medical, Walnut Creek, CA, USA). Fast Red (Biocare Medical) was used to develop the colorimetric reactions. Sections were counterstained with hematoxylin and mounted with glycerol jelly. The samples were evaluated under a bright-field microscope (Eclipse 90i, Nikon). Negative and isotype-matched control sections were evaluated.

Live and dead assay was performed on hMSCs, the nuclear components of which were then counterstained with 1 μ g/mL of 4',6-diamidino-2-phenylindole, dihydrochloride (Sigma-Aldrich) at RT for 5 min. We evaluated the cells with a DS-Ri2 microscope (Nikon, Tokyo, Japan), containing NIS-Elements Software (Nikon, Tokyo, Japan).

2.7.5. Statistical Analyses. Statistical analyses were performed using GraphPad Prism 8 software (San Diego, CA, USA). Normal distribution and homogeneity of variance were evaluated using the Shapiro–Wilk test and the Levene test, respectively. The data obtained were evaluated with Kruskal–Wallis and Dunn's multiple comparison tests. * $p < 0.05$ and ** $p < 0.01$ were considered significant. Data were represented as the average value \pm standard deviation (average value \pm SD).

3. RESULTS AND DISCUSSION

3.1. Rheological Characterization. The rheological characterization of bioinks involved in this study is shown in Figure 1, where the shear–viscosity profiles are reported.

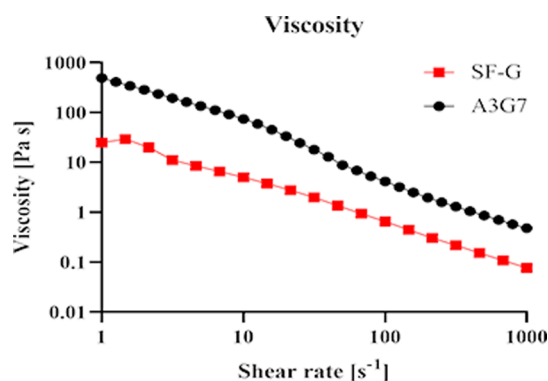


Figure 1. Viscosity trend of SF-G (red) and A3G7 (black) bioinks in log–log scale for shear rates from 1 to 1000 s^{-1} .

Evaluating the viscosity and shear rate, it was possible to observe that the bioinks are shear-thinning fluids, characterized by a decrease in viscosity over an increasing shear rate. To obtain the quantification of the degree of shear-thinning, the linear trends were determined by plotting the results on log–log scale axes (Figure 1) and verified by applying the power-law regression, as previously described.²¹ The power-law regression applied to the pseudoplastic fluids showed an R^2 value of 0.9978 and 0.9714 for the SF-G and A3G7 bioinks, respectively. Moreover, the linear region was identified in the

shear rate range between 1.0 and 1000 s^{-1} . A shear rate value in the linear region was chosen to obtain the power-law index (n) through a curve-fitting procedure. The calculated values were 0.1697 and 0.1103, respectively, for the SF-G and A3G7 bioinks. The results were in accordance with our previous rheological evaluations,³⁸ and they showed that bioinks were pseudoplastic fluids.⁴⁰

The viscosity of the SF solution was 0.002 Pa·s at a shear rate of 200 s^{-1} , as previously reported.³⁴ It remains constant by varying the shear rate, while the viscosity for the SF-G cross-linked blend with mushroom tyrosinase at the same shear rate increased to 1.71 Pa·s⁴⁶ and showed a decreasing trend. After 20 min from the enzyme addition, the rheological properties of the SF-G bioink resulted in stable ink and could be used to print 3D structures, since it demonstrated a shear-thinning behavior and showed a higher viscosity. Also, the A3G7 bioink showed a stable viscosity when the temperature was kept at 25 $^{\circ}$ C over time.

The model developed in this study applies only to shear-thinning bioinks. Pristine SF solutions showed a Newtonian fluid-like behavior,³¹ whereas G had a temperature-dependent behavior (without shear-thinning properties). Therefore, raw materials are not printable as individual components, and the model reported in this paper cannot be applied to them.

3.2. Model Outputs. The model was run to predict the deposition filament widths of SF-G and A3G7 bioinks for all the selected combinations of v and P using three different needle lengths and three needle diameters for each length, as described in Section 2.5. The filament width values predicted by the analytical model using the D0.20_L6.35 needle are reported on the 3D plot graphs in Figure 2a for the SF-G bioink and in Figure 2b for the A3G7 bioink. All graphs of the other needles used in the analytical model are shown in Figure S2 (D0.20), Figure S3 (D0.41), and Figure S4 (D0.50) for the SF-G bioink and in Figure S5 (D0.20), Figure S6#sifile1 (D0.41), and Figure S7 (D0.50) for the A3G7 bioink. All numerical values are shown in Tables S1 and S2. Figures S2–S7 summarize the 3D plot graphs reporting the analytical filament widths obtained as a model output and applied to the needles tested using the SF-G and A3G7 bioinks, respectively. It can be observed that the 3D surface maintained the same shape for each bioink derived by the implemented model equation in which the different colors correspond to different filament widths (increasing from blue to red). In general, the filament width increased with the printing pressure and decreased with the printing speed. However, the diameter and the length of the needles also influenced the output. The maximum widths for the SF-G bioink using 3×10^5 Pa and 0.5×10^{-3} m/s (the combination of printing pressure and speed to have the maximum material deposition) were 388, 304, and 244 μ m for D0.20_L6.35, D0.20_L12.7, and D0.20_L25.4 needles, respectively; 1210, 856, and 605 μ m for D0.41_L6.35, D0.41_L12.7, and D0.41_L25.4 needles, respectively; 1800, 1273, and 900 μ m for D0.50_L6.35, D0.50_L12.7, and D0.50_L25.4 needles, respectively. For the same diameter, the width decreased by increasing the length, and for the same length, the width increased by increasing the diameter. In the case of the A3G7 bioink, as shown in Table S2, the maximum values were smaller than the corresponding values of the SF-G bioink due to the higher viscosity of the blend.

In a previous work,⁴² the authors have shown only a plot of the filament width versus the printing speed, without

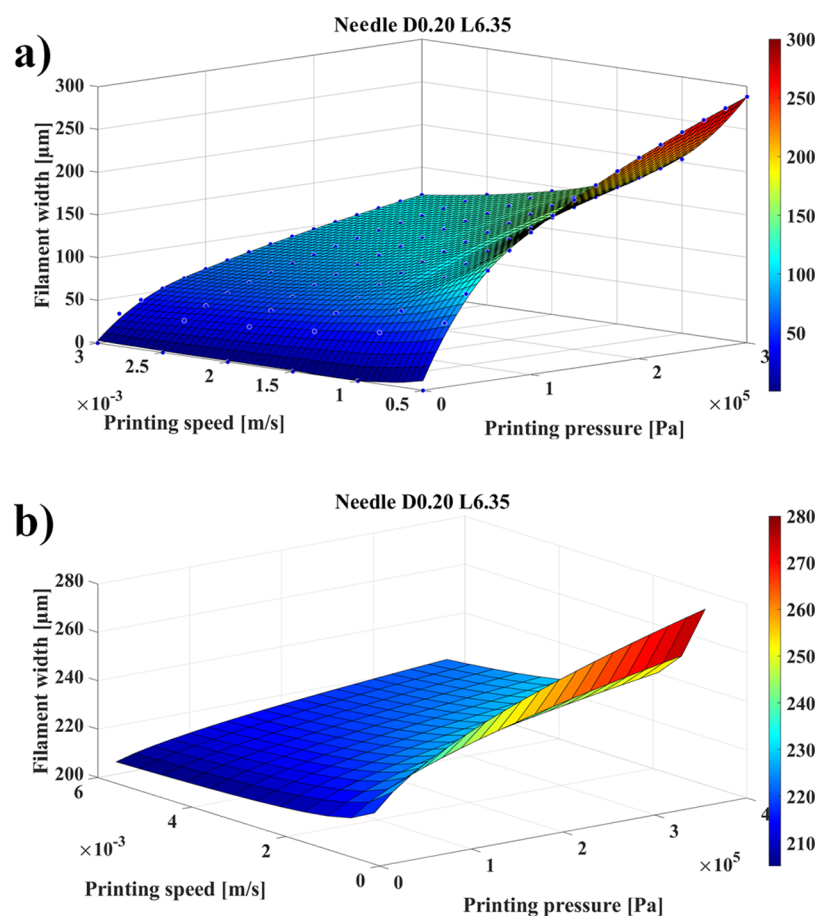


Figure 2. Three-dimensional graph representations of the analytical filament width of D0.2_L6.35 needle for SF-G (a) and A3G7 (b) bioinks related to printing pressure (x -axis, $\times 10^5$ Pa) and printing speed (y -axis, $\times 10^{-3}$ m/s). All 3D graphs about the analytical filament width of other needles related to SF-G and A3G7 bioinks are shown in Figures S2–S4 and S5–S7, respectively.

correlating it with the needle diameter. The selection of the needle for hydrogel printing should aim to reproduce a filament width equal to the needle diameter. For this reason, the selected printing speed was directly correlated to the printed filament using a certain needle. The filament width varies depending on the needle diameter if the average extrusion velocity is similar to the printing speed. However, it has been shown that the relation between filament width and needle diameter occurs only if the volume of the material flowing through the needle precisely retained the filament thickness.²¹ The balance between the printing speed and flow is crucial to have a well-defined extruded filament through the needle. If the printing speed is too low concerning the material flow velocity to exit from the needle, too much material is extruded, and consequently, nondefined structures could be printed as they lose the microarchitecture. Conversely, with a high printing speed, insufficient material can be extruded from the needle and no printed structures could be obtained. Regarding this goal, the potential of the analytical model is that it provides a prior knowledge of the range of printing parameters that can be used with certain needles.⁴⁷ Concerning previous state-of-the-art efforts,^{21,42} in this study, we report for the first time an analytical model to predict the optimal printing parameters to achieve the desired deposited filament width given the rheological parameters, the printing pressure, the printing speed, the needle diameter, and the needle length, for this type of hydrogels and in their printability window. Moreover, we have applied the model to

a large range of needles with different diameters (from 0.05 to 1.00 mm) and lengths (from 6.35 to 25.4 mm) to confirm that it can be used for other needles not tested in this study. However, the model must be always contextualized with the available printing parameters of the bioprinter used to deposit a bioink with particular rheological properties. For example, if the bioink has a high viscosity, the pressure needed to extrude a filament can overcome the maximum one that can be applied by the bioprinter. Thus, the model may allow performing a preliminary screening of bioinks, needles, and bioprinter parameters. Moreover, in the case of bioprinting procedures with embedded cells, it can be used to predict if excessive printing pressure is applied, which may imply cell damages.

3.3. Experimental Validation. The percentage error values of SF-G and A3G7 are respectively shown in Tables S3 and S4. The nonprintable conditions are defined as N.A. (not available) (Tables S3, S4, and Figure S8a), and the cases without a well-defined internal microstructure are defined as “blob” (Tables S3, S4, and Figure S8c). They are both compared with well-defined structures with finite extruded filament widths (Figure S8b). The nonprintable conditions occurred when the pressure was too low or when the printing speed was too high. By contrast, the blob conditions occurred when a high pressure or a low printing speed was used, determining a large amount of bioink deposition. Moreover, in Tables S3 and S4, the orange and green colors identify, respectively, the underestimated and overestimated errors with regard to the deposited filament widths.

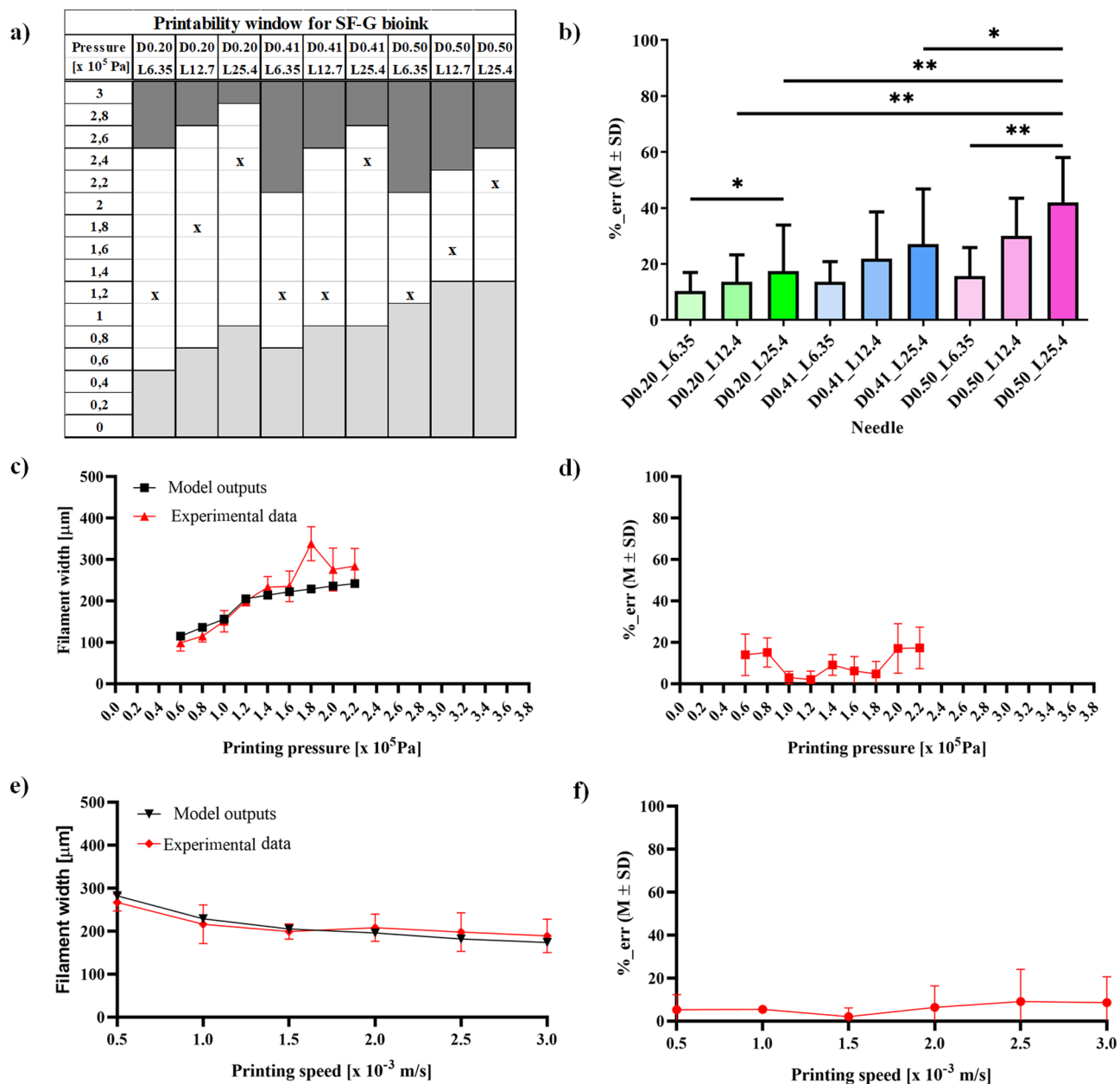


Figure 3. (a) Printability window of the SF-G bioink for all the needles tested (the white portion with the “x” symbol represents the best printing conditions to have a filament width equal to the needle diameter; the dark gray portion represents blob conditions, and the light gray portion represents nonprintable conditions). (b) Average error between the analytical model and experimental printing data, for all needles. (c) Comparison between model outputs and the acquired experimental data for the SF-G bioink printed using a D0.20_L6.35 needle at $v = 1.5 \times 10^{-3}$ m/s and varying the printing pressure with steps of 0.2×10^5 Pa. (d) Corresponding error values vs printing pressure for the D0.20_L6.35 needle at $v = 1.5 \times 10^{-3}$ m/s between model outputs and experimental data. (e) Comparison between model outputs and the acquired experimental data for the SF-G bioink printed using the D0.20_L6.35 needle at $P = 1.2 \times 10^5$ Pa and varying the printing speed with steps of 0.5×10^{-3} m/s (f) corresponding error values vs printing speed for the D0.20_L6.35 needle at $P = 1.2 \times 10^5$ Pa between the model outputs and experimental data. Data are expressed as average value \pm SD (* $p < 0.05$, ** $p < 0.01$).

The distance between the printing needle tip and the bed surface is an important printing parameter to consider for obtaining a suitable deposition process. The choice of the right needle height is crucial to have a controllable filament width, and it is strictly dependent on the other printing parameters (P , v , and needle characteristics). If the initial height is short, the deposited filament results too swollen. On the other hand, if the initial height is too high, the filament cannot adhere to the bed surface. In the present study, we adopted a criterion reported by Paxton *et al.*,²¹ where the initial height was set to

$2/3$ of the needle diameter to print the first layer of the 3D structure, obtaining a suitable filament deposition.

Moreover, the bioprinter internal temperature was kept at 21 ± 1 °C during the printing process of SF-G and 25 ± 1 °C during the printing process of A3G7, and the printing bed surface was always kept at RT to avoid the swelling of the deposited filament. The temperature influences the filament width when interacting with the bed surface. It was demonstrated that the synthetic filament of acrylonitrile-butadiene-styrene and polylactic acid deposited on the glass

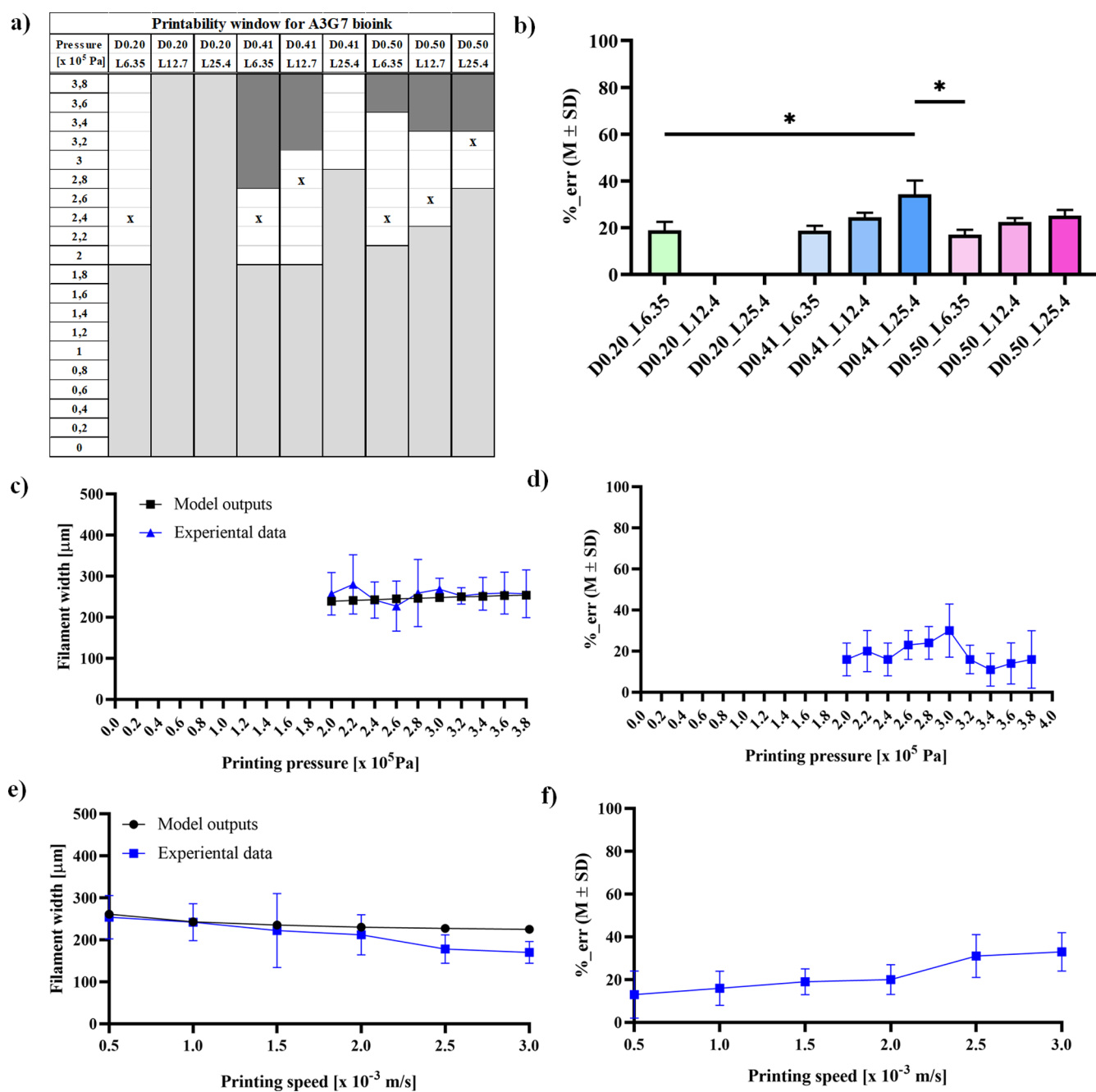


Figure 4. (a) Printability window of the A3G7 bioink for all the needles tested (the white portion with the “x” symbol represents the best printing conditions to have a filament width equal to the needle diameter, the dark gray portion represents blob conditions, and the light gray portion represents nonprintable conditions). (b) Average error between the analytical model and experimental printing for all needles. (c) Comparison between model outputs and the acquired experimental data for the A3G7 bioink printed using the D0.20_L6.35 needle at $v = 1.0 \times 10^{-3}$ m/s and varying the printing pressure with steps of 0.2×10^5 Pa. (d) Corresponding error values vs printing pressure for the D0.20_L6.35 needle at $v = 1.0 \times 10^{-3}$ m/s between model outputs and experimental data. (e) Comparison between model outputs and the acquired experimental data for the A3G7 bioink printed using the D0.20_L6.35 needle at $P = 2.4 \times 10^5$ Pa and varying the printing speed with steps of 0.5×10^{-3} m/s (f) corresponding error values vs printing speed for the D0.20_L6.35 needle at $P = 2.4 \times 10^5$ Pa between model outputs and experimental data. Data are expressed as average value \pm SD (* $p < 0.05$, ** $p < 0.01$).

surface at two different temperatures showed a higher adhesion due to the increased material contact area.⁴⁸ Also, in the case of natural polymers such as SF–G bioink, the deposited filament increased its contact area with the above glass, thus increasing the bed surface temperature. Additionally, after printing, the filament shape can assume a circle or a half-ellipse shape determined by the balance of bioink properties (i.e.,

interfacial tension) and interfacial interaction with the surface (e.g., air and contact surface).

As shown in Figure 3a, we evidenced with white the printing window of the SF–G bioink that can produce well-defined structures, for each needle and pressure range. Pressure values too low and too high were evidenced with light and dark gray colors, respectively. We observed that the starting pressure of the printing window increased with the needle lengths and

diameters. By contrast, the minimum pressure to have blob conditions decreased with increasing needle diameters and lengths. Following this trend, the printability window becomes narrower, using larger and longer needles. To our knowledge, this is the first time that the printability window is characterized considering both the diameter and length of the needles (it was made in the state of the art, considering only one parameter).²¹ To demonstrate the relevance of the analytical model in realistic printing conditions using the SF-G bioink, we demonstrated that for every needle, the optimal parameters, to obtain a filament with a similar width as the needle diameter, were within the window of printability (the white portions indicated with “x” symbols in Figure 3a). The limit for the SF-G-based hydrogel bioink was the narrow printability window due to the enzymatic cross-linking method. Indeed, the rheological properties of the SF-G-based hydrogel bioink were stable for approximately 1 hour after enzymatic cross-linking activation (the cross-linking reaction started approximately 20 min later).³⁸ The viscosity of the SF-G bioink increased with time but mainly after enzyme addition. As reported in our previous work,³⁸ the viscosity became stable after 12 min of the enzyme addition. After 24–72 min from enzyme addition, the viscosity was found to be between 1.2 and 1.3 Pa·s at 100 s⁻¹.

However, the limited printability window of the SF-G bioink was acceptable, considering that longer printing time windows may hamper cell survival during the fabrication process. Interestingly, within the SF-G bioink printability time window, the process was well reproducible, allowing to print dozens of 3D structures that retain the fidelity of the target design.

With regard to the calculated errors between the analytical model and the experimental printing process, the average error measured for each needle and all pressure and printing speed ranges were measured, using only the values inside the respective printability windows. Figure 3b–d shows that the average errors of each needle were lower than 20% in all cases except for the D0.50_L12.7 and D0.50_L25.4 needles due to the large amount of material that was extruded in these cases, and it was due to the low shape retention of the SF-G bioink. In general, we observed that the error increased with the increase of needle diameter and length. When the needle length increased from 6.35 and 25.4 mm, statistical differences were found between D0.20_L6.35 and D0.20_L25.4 needles (**p* < 0.05) and between D0.50_L6.35 and D0.50_L25.4 needles (***p* < 0.01) at fixed needle diameters. Moreover, the needles with the same length and a larger diameter showed an increased average error. In Figure 3b, statistical differences were found to be also between D0.20_L12.7 and D0.50_L12.7 needles (**p* < 0.01), D0.20_L25.4 and D0.50_L25.4 needles (**p* < 0.01), and D0.41_L25.4 and D0.50_L25.4 needles (**p* < 0.05) when the diameter increased and length was fixed. Using longer needles implied higher errors. A possible explanation of this phenomenon is that, when using longer needles, the bioink is affected by higher internal shear rates that determine the extrusion of a larger filament. It could be interesting in future works to compare the deformation of non-Newtonian fluids inside different needles (in terms of D and L), coupling these observations with CFD analyses.

With regard to the chosen needle (D0.20_L6.35), as reported in Figure 3c, the experimental data followed the model outputs with varying printing pressure, maintaining fixed the printing speed at 1.5 × 10⁻³ m/s. However, larger

widths were measured from 1.8 and 2.2 × 10⁵ Pa due to the high pressure extruding a considerable amount of bioink. Figure 3d shows the corresponding error trend. The values were always under 20% and were slightly smaller in the middle of the pressure range (1.0–1.8 × 10⁵ Pa). Figure 3e shows the comparison between model outputs and experimental data, maintaining fixed pressure at 1.2 × 10⁵ Pa and evaluating all printing speeds. No significant differences were observed. The error trend (Figure 3f) remained constant and low. The minimum error was observed at 1.5 × 10⁻³ m/s. All printed constructs' images are shown in Figure S9a (varying the printing pressure) and in Figure S9b (varying the printing speed). The calculated error percentages for all needles are reported in Table S3, in which the colors indicate if the model underestimated (orange) or overestimated (green) the filament width.

Therefore, the measured error was considered reasonable due to the common swelling behavior of hydrogels after printing. To our knowledge, in the literature, no reports have established an error cutoff value that can be considered suitable to validate the analytical models, considering the percentage of error between the model and experimental outputs. Finally, we evidenced that the error values followed the analytical model outputs, and the experimental printing process provided information about nonprintable and blob conditions to choose the optimal printability window.

To further validate the proposed model, a similar assessment was also carried out on the A3G7 bioink. In Figure 4a, the printability windows for all the needles tested are shown. It can be observed that printability is achieved at higher pressure values concerning the SF-G bioink, due to the higher viscosity of A3G7. For this reason, it was not possible to print the A3G7 bioink through the D0.20_L6.35 and D0.20_L12.7 needles. The printing pressure needed to obtain a filament having a width similar to the needle diameter was marked in the white portions with “x”. Figure 4b reports the errors between the analytical model predictions and the experimental values obtained during the printing process, for each needle. The error values for the A3G7 bioink resulted slightly larger compared to the SF-G ones. However, as for the SF-G bioink, the error increased with the needle length. Statistically significant differences were found between D0.20_L6.35 and D0.41_L25.4 (*p* < 0.05) and between D0.51_L6.35 and D0.41_L25.4 (*p* < 0.05). Figure 4c shows the difference between the model outputs and the experimental values, for a D0.20_L6.35 needle, at a printing velocity of 1.0 × 10⁻³ m/s and different printing pressures. Figure 4d shows the corresponding error values. It can be observed that the error increased slowly with the printing pressure until the value of 3.0 × 10⁵ Pa.

Finally, Figure 4e,f shows the comparison between the model outputs and the experimental data and the corresponding error values, respectively, for a D0.20_L6.35 needle at a printing pressure of 2.4 × 10⁵ Pa and different printing speeds. Larger deviations from the model were observed for speeds ranging from 2.0 to 3.0 × 10⁻³ m/s. Indeed, the relatively high viscosity of A3G7 negatively affected its printability at high speeds. Pictures of the corresponding printed constructs are shown in Figure S10a (varying the printing pressure) and in Figure S10b (varying the printing speed). The calculated error percentages for all needles are reported in Table S4, where the colors indicate if the model underestimated (orange) or overestimated (green) the filament width.

For the biological characterization of SF–G, the D0.20_L6.35 needle was chosen to print the widest filament. Keeping constant the interfilament distance at 1.00 mm, the porosity (ratio between empty volume and filled volume) of 3D structures was at least 80% in dry conditions (following these design parameters, we obtained a porosity of 83.34%).^{16,17,49,50} The open 3D structure can promote an improved diffusion of nutrients to keep cells healthy during the chondrogenic differentiation period. The long-term evaluation of the printed filament in wet conditions may be affected by hydrogel filament swelling due to hydration produced by the culture medium.^{50,51}

To obtain filaments with widths similar to the needle diameters, the printing parameters were found correlating with calculated errors and are shown in Tables S3 and S4 for both bioinks. The pressures fall inside the printability window of needles, as shown in Figures 3a and 4a. Supposing that the needle with the smallest length produced the smallest shear stress to the embedded cells, the needle with 6.35 mm length (D0.20_L6.35) was chosen to print the SF–G-based 3D constructs.

The printing parameters were chosen within the printability window, considering both the minimum error percentage and the minimum pressure needed to guarantee the best filament extrusion and optimal cell survival. Moreover, the selected diameter of 0.2 mm permitted to have an accurate filament deposition and a high porosity of the 3D structures within the design of filling pattern (interfilament design), ensuring nutrient diffusion for cell viability and functions like chondrogenic differentiation through the whole structure depth.

Although this study did not focus on constructs' mechanical properties, it is worth mentioning that a precise control over the construct microarchitecture can also enable the modulation of the constructs' mechanical properties (e.g., by producing anisotropically aligned fibers or other patterns).⁵² This gives value to the findings obtained in this work, which help to correctly predict the filament geometrical features for a wide range of conditions, thus highlighting a possible impact on the precise control of construct microarchitectures and thus mechanical properties.

The model used in this study was already presented by Suntuornond and coauthors.²⁴ Indeed, they proposed a model to predict the width of a printed synthetic hydrogel line as a function of nozzle size, printing pressure, and speed. The novelty of our work concerns the application of such a model to natural polymer-blended bioinks, which are highly promising for the tissue engineering of musculoskeletal tissues. The model was tested on two gelatin-based bioinks blended with SF and alginate, which are among the most common natural materials used in this research field. The application of the abovementioned already existing model to natural polymers was not straightforward as known; some common models exist that describe the behavior of both synthetic and natural hydrogels. However, it is also known that even hydrogels showing similar rheometric properties (e.g., non-Newtonian ones) often differ in their adherence to such models, due, for example, to slight differences in crystallinity, physical entanglement mechanisms, and other chemical–physical features. This applies to models concerning cross-linking, transport properties, drug delivery kinetics, and so forth.^{53,54} Bioprinting models based on material rheological properties have been proposed and validated for some

synthetic hydrogels but never for natural polymer-blended bioinks. Our results demonstrate that these models can also be used with this material type. Furthermore, having validated the model with different natural blends, this study allows somehow to generalize the considerations derived from the results obtained.

3.4. Shear Stress Values. The experimental shear stress was estimated to validate the hypothesis that the needle with the smallest length produces smaller shear stresses to cells at the same applied pressure and to select the most appropriate needle. We estimated the shear stress acting on the needles having a 0.2 mm diameter, to evaluate if cell viability could be guaranteed, using different pressures. As shown in Figure 5, the

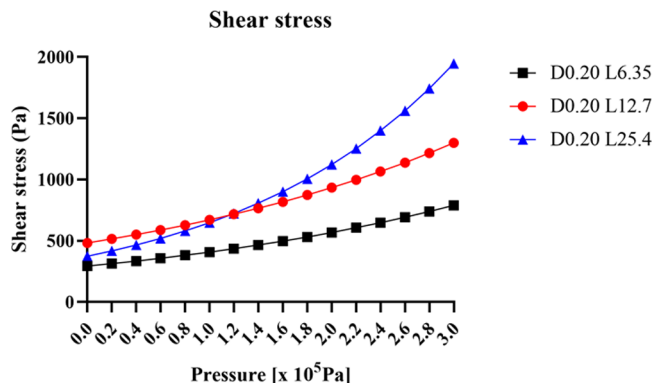


Figure 5. Shear stress trends (y-axis, Pa) within needles with a diameter of 0.2 mm and different lengths (6.35, 12.4, and 25.4 mm) calculated for the printing pressure range (x-axis, 0–3 $\times 10^5$ Pa, with steps of 0.2×10^5 Pa) of SF–G bioink.

shear stress increased with the pressure and the length of the needle used, but it was always smaller than 2 kPa, in the range of pressures considered (up to 3×10^5 Pa). To use the minimum pressure value to print $200 \mu\text{m}$ filaments, the needle with a 6.35 mm length was the best choice to have the smallest shear stress.

As previously shown, 1.2×10^5 Pa was the optimal pressure guaranteeing a suitable printing performance, according to the experimental findings obtained during the model validation phase. In correspondence to such a pressure value, the selected needle (D0.20_L6.35) showed a maximum shear stress value that was 436 Pa, in line with previous reports highlighting this parameter as safe for cells.⁴¹ Finally, based on the model, we found that the shear stress values corresponded to the optimal printing parameters for producing $200 \mu\text{m}$ wide filaments; instead, using the other needles, the filament widths were about 800 and $1140 \mu\text{m}$ at pressures of 1.8×10^5 and 2.0×10^5 Pa (Table 2). Theoretically, the cell viability was ensured by shear stress evaluation.^{41,55,56}

Our data showed that the calculated shear stress of the cylindrical shaped needles was lower than 5 kPa,⁴¹ for all pressures and needle lengths considered and using a 0.2 mm needle diameter, which ensured good viability. Moreover, the use of cylindrical shaped needles can help to print a low-viscosity hydrogel as SF–G, limiting material flow and enhancing the printing fidelity. However, the use of conical shaped needles considerably decreases the pressure used during the filament deposition, with an advantage in terms of shear stress on the cells.⁵⁷ This is an important preliminary evaluation that must be considered in the case of high-viscosity

Table 2. Printing Parameters to Print Filaments Equal to Needle's Diameters for Both SF-G and A3G7 Bioinks

needles ID	D [mm]	L [mm]	SF-G bioink				A3G7 bioink			
			d_{exp} [μm]	% _{err}	P [$\times 10^5$ Pa]	v [$\times 10^{-3}$ m/s]	d_{exp} [μm]	% _{err}	P [$\times 10^5$ Pa]	v [$\times 10^{-3}$ m/s]
D0.20_L6.35	0.20	6.35	196	2.1	1.2	1.5	212	14.6	2.4	1.0
D0.20_L12.7	0.20	12.7	191	4.3	1.8	1.5	-	-	-	-
D0.20_L25.4	0.20	25.4	195	9.6	2.4	1.5	-	-	-	-

material to have a process with viable printed cells (results not shown).

3.5. Bioprinting and Cell Viability. Microscopic analyses of the printed construct evidenced a well-defined micro-architecture with open pores, good interconnectivity, and a homogeneous distribution of the cells into the SF-G hydrogel construct filaments (Figure 6a). The deposited SF-G-based

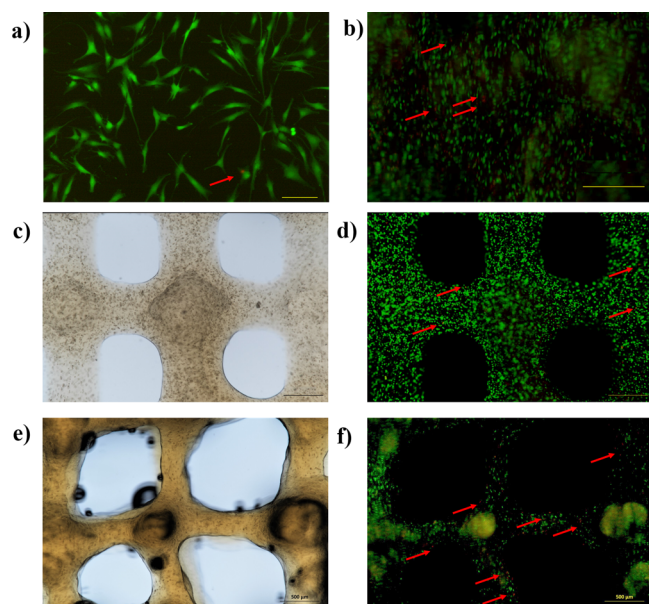


Figure 6. Representative images of cell morphology and viability of SF-G hydrogels printed with a D0.20_L6.35 needle. (a) hMSCs before encapsulation in SF-G hydrogel show a spindle-shaped morphology and high cell viability; (b) hMSC-laden SF-G bioink before printing; (c, d) morphological cell distribution and cell viability into the postprinted filament (scale bar = 200 μm); (e, f) morphological cell distribution and cell viability embedded into the filament after 28 days (green = viable cells, red = dead cells, scale bar = 500 μm). Red arrows evidence dead cells.

filament with embedded cells showed a width of $238 \pm 26 \mu\text{m}$ with a small difference concerning the analytical model output for the printing parameters used for the D0.20_L6.35 needle (see Table 2).

hMSCs showed a high percentage of cell viability (95%) in monolayer culture before their encapsulation within the bioink (Figure 6a) and after their encapsulation into the bioink, before performing the bioprinting process (Figure 6b). Live and dead assay confirmed that almost all the cells (more than 90%) were viable (green cells) and only a few cells were dead (red cells, less than 10%) (Figure 6d). A similar trend in the cell viability was confirmed after 28 days of printing (Figure 6f).

The selected design parameters allowed to achieve open and interconnected pores after printing (Figure 6c), which continued even after 28 days (Figure 6e). It has been shown

in previous reports that cells embedded within a hydrogel were found to be viable after printing if the applied shear stress was lower than 5 kPa.⁴¹ The printing process used in this study was featured by shear stress smaller than such a threshold (~ 436 Pa). Cell viability was ensured using cylindrical shaped needles, even if other authors reported that conical shaped needles may contribute to decreasing cell mortality during the printing process.⁵⁸

3.6. Immunohistochemical Analyses. Immunohistochemical analyses of SOX9 and collagen type 2 markers confirmed that the chondrogenic differentiation of hMSCs occurred in SF-G-based 3D structures (in the presence of TGF- β 3), as previously published²⁵ (Figure 7). On day 28, the differentiation was associated with an increase of SOX-9, the specific chondrogenic transcriptional factor, as well as of collagen type 2, the main cartilage-specific ECM,^{59–62} confirming that the hydrogel created an appropriate micro-environment for hMSCs' chondrogenic differentiation.

Interestingly, we observed that until day 28, the micro-architecture of the construct maintained a well-defined structure with open pores and good interconnectivity, only in chondrogenically differentiated constructs. This micro-architecture was partially lost in the control condition, for which we observed the presence of proliferating cells into the pores. In the control condition, the construct was not treated with TGF- β 3, which is known to contribute to chondrogenic differentiation and ECM production, that also contributes toward the maintenance of the 3D structure with embedded cells. SF-G-based constructs showed good shape retention. Their excellent biological activity has been widely exploited in the field of cartilage tissue engineering.^{27,29,38,63,64} These results suggest that the defined analytical model parameters favored the printing of 3D constructs that retained their structure until day 28, only when hMSCs were cultured in chondrogenic conditions, suggesting that the collagen matrices, produced by chondrogenic differentiated cells, contributed to maintaining the printed structure. In the control condition, the enhanced proliferation of hMSCs inside the pores could have contributed to affect the design of the printed construct. It has been shown that mechanical properties directly influence cell morphology, migration, and differentiation, thus guiding tissue regeneration.^{65–68} In this view, future studies focusing on mechanobiology, in which the modulation of mechanical properties and the corresponding cell functions may be evaluated, may benefit from the predicting tool and the results reported in this paper. Indeed, knowing the conditions for reliable printing and control of filament width can surely have an impact on the fine control of the construct micro-architecture (and thus mechanical properties).

4. CONCLUSIONS

Extrusion-based 3D bioprinting strategies are widely used to produce cell-laden hydrogel constructs. This approach enables the fabrication of constructs able to maintain cells alive and to drive their phenotypes to regenerate tissues. Nowadays, efforts

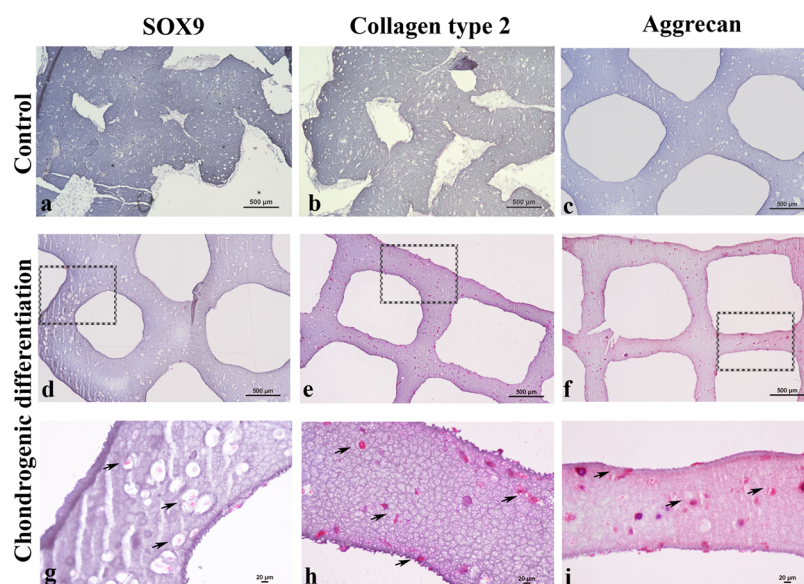


Figure 7. Immunohistochemical analysis of SOX-9 (a, d, g), collagen type 2 (b, e, h), and aggrecan (c, f, i) on both control and chondrogenically differentiated (+TGF- β 3) hMSCs, laden in SF-G-based printed constructs after 28 days. Scale bars = 500 (a–f) and 20 μ m (g–i). Square areas in images (d–f) are shown at higher magnification in images (g–i). Black arrows evidence positive stained cells (in red).

in this field are mainly driven by experiments and trial-and-error approaches, leading to time and material loss, as well as to a lack of reliability and repeatability of the printing process outcomes. To predict the deposited filament of natural-based bioinks through extrusion-based 3D bioprinting, an analytical model²⁴ was developed, considering as the input key printing process parameters such as pressure and speed for a selected range of needle sizes. The main advantage of this model is the possibility to start from the various rheological properties of different hydrogels for predicting the filament width, thereby helping researchers to define the most suitable printing parameters to maximize the fidelity of the fabricated constructs to design parameters. The SF-G and A3G7 bioinks presented the typical viscosity behaviors of shear-thinning fluids and could be printed with pneumatic systems. The viscosity followed a power law in the linear scale and the linear trend in the log–log scale. Therefore, the rheological parameters (K and n) were used as inputs into the model to predict the width of the deposited filaments. The model permitted to extrapolate results in terms of the printed filament width at varying printing parameters (pressure and speed) and needle characteristics (length and diameter). Therefore, the filament width prediction was used to print a 200 μ m filament to have SF-G-based 3D structures with acceptable porosity. The structure design was chosen to obtain a good nutrient diffusion through 3D constructs despite a foreseeable swelling of the material. The good nutrient diffusion in MSCs encapsulated in SF-G was able to ensure optimal cell viability from postprinting to day 28 in culture conditions. Previous proteomic analyses demonstrated the impact of SF on the chondrogenic potential of MSCs embedded in SF-G. These cells cultured with TGF- β 3 generated a stable chondrogenic phenotype by exhibiting typical collagens and filamin b of in vivo articular cartilage. Moreover, none of the collagens related to hypertrophy were noticed in the constructs after TGF- β 3 addition. Notably, the proteomic analysis gave evidence of the activation of typical anabolic signaling pathways like Wnt, Notch, and HIF-1 promoting cartilage repair.⁶⁹ Moreover, the printing process did not affect cell viability, and the hMSCs

produced cartilaginous ECM that is confirmed by positive chondrogenic markers after 28 days. However, further biological evaluations (i.e., mechanical properties) are necessary to find out the biological potentiality of this construct.

In conclusion, the testing of this analytical model allows predicting the printing conditions starting from their hydrogel rheological properties used for the regeneration of target tissues, like the osteochondral unit. The proposed analytical model contributes to better guarantee controlled and standardized conditions (than classical approaches) useful to optimize tissue engineering approaches targeting several applications in regenerative medicine.

Overall, the use of the proposed analytical model allows to identify the optimal printing parameters to maximize the fidelity of the fabricated constructs with respect to the proposed design. This enables more controlled and standardized biofabrication products. The limitation of this model is that it does not provide direct information on the printability window, and so some preliminary tests are still required for the process. Anyhow, this model contributes to reduce the number of experimental steps as well as of the required materials and the time consumption. Moreover, by including an evaluation of the applicable shear stresses and how to select printing parameters, the model also provides useful indications on how to avoid postprinting cell viability loss that represents a subtler and less detectable failure mechanism for the bioprinting process. Therefore, the models that use as an input the rheological properties of the hydrogel might be a valid tool for optimizing TE approaches.

■ ASSOCIATED CONTENT

Supporting Information

The Supporting Information is available free of charge at <https://pubs.acs.org/doi/10.1021/acsbiomaterials.1c00410>.

Photograph of a camera setup for measuring the extruded filament; 3D graph representations of analytical filament width for SF-G and A3G7 bioinks related to

printing pressure and printing speed; photographs of the unprinted condition of the well-defined structure and of case without well-defined internal microstructure (blob); photographs of SF-G and A3G7 printed bioinks varying the printing pressure and fixing the printing speed and vice versa; photographs of the first and the last printed SF-G structures during the same bioprinting process; filament width for SF-G and A3G7 bioinks calculated using the analytical deposition model; and percentage error values width for SF-G and A3G7 bioinks calculated by using the analytical deposition model (PDF)

AUTHOR INFORMATION

Corresponding Authors

Sourabh Ghosh – Regenerative Engineering Laboratory, Department of Textile Technology, Indian Institute of Technology, 110016 New Delhi, India; Email: Sourabh.Ghosh@textile.iitd.ac.in

Gina Lisignoli – IRCCS Istituto Ortopedico Rizzoli, SC Laboratorio di Immunoreumatologia e Rigenerazione Tissutale, 40136 Bologna, Italy; orcid.org/0000-0003-2837-9967; Email: gina.lisignoli@ior.it

Authors

Diego Trucco – IRCCS Istituto Ortopedico Rizzoli, SC Laboratorio di Immunoreumatologia e Rigenerazione Tissutale, 40136 Bologna, Italy; The BioRobotics Institute and Department of Excellence in Robotics & AI, Scuola Superiore Sant'Anna, 56127 Pisa, Italy

Aarushi Sharma – Regenerative Engineering Laboratory, Department of Textile Technology, Indian Institute of Technology, 110016 New Delhi, India

Cristina Manferdini – IRCCS Istituto Ortopedico Rizzoli, SC Laboratorio di Immunoreumatologia e Rigenerazione Tissutale, 40136 Bologna, Italy

Elena Gabusi – IRCCS Istituto Ortopedico Rizzoli, SC Laboratorio di Immunoreumatologia e Rigenerazione Tissutale, 40136 Bologna, Italy

Mauro Petretta – IRCCS Istituto Ortopedico Rizzoli, Laboratorio RAMSES, 40136 Bologna, Italy; RegenHu Ltd., CH-1690 Villaz St. Pierre, Switzerland; orcid.org/0000-0002-8803-7013

Giovanna Desando – IRCCS Istituto Ortopedico Rizzoli, Laboratorio RAMSES, 40136 Bologna, Italy

Leonardo Ricotti – The BioRobotics Institute and Department of Excellence in Robotics & AI, Scuola Superiore Sant'Anna, 56127 Pisa, Italy; orcid.org/0000-0001-8797-3742

Juhi Chakraborty – Regenerative Engineering Laboratory, Department of Textile Technology, Indian Institute of Technology, 110016 New Delhi, India

Complete contact information is available at:

<https://pubs.acs.org/10.1021/acsbomaterials.1c00410>

Notes

The authors declare no competing financial interest.

ACKNOWLEDGMENTS

This work was funded by the Executive Programme for Scientific and Technological Cooperation between the Italian Republic and the Republic of India (2017–2019, N.

IM17MO03) and Rizzoli fund “5 × 1000”. It was also supported by the European Union’s Horizon 2020 research and innovation program, grant agreement no 814413, project ADMAIORA (Advanced nanocomposite MaterIals fOr in situ treatment and ulTrAsound-mediated management of osteoarthritis). The authors also acknowledge Martina Puricelli for her collaboration during the preliminary work.

REFERENCES

- (1) Murphy, S. V.; Atala, A. 3D bioprinting of tissues and organs. *Nat. Biotechnol.* **2014**, *32*, 773.
- (2) Heinrich, M. A.; Liu, W.; Jimenez, A.; Yang, J.; Akpek, A.; Liu, X.; Pi, Q.; Mu, X.; Hu, N.; Schiffelers, R. M.; Prakash, J.; Xie, J.; Zhang, Y. S. 3D Bioprinting: from Bench to Translational Applications. *Small* **2019**, *15*, 1805510.
- (3) Xia, Z.; Jin, S.; Ye, K. Tissue and Organ 3D Bioprinting. *SLAS Technol.* **2018**, *23*, 301.
- (4) Mandrycky, C.; Wang, Z.; Kim, K.; Kim, D.-H. 3D bioprinting for engineering complex tissues. *Biotechnol. Adv.* **2016**, *34*, 422–434.
- (5) Ong, C. S.; Yesantharao, P.; Huang, C. Y.; Mattson, G.; Boktor, J.; Fukunishi, T.; Zhang, H.; Hibino, N. 3D bioprinting using stem cells. *Pediatr. Res.* **2018**, *83*, 223–231.
- (6) Jiang, L.; Wang, Y.; Liu, Z.; Ma, C.; Yan, H.; Xu, N.; Gang, F.; Wang, X.; Zhao, L.; Sun, X. 3D Printing and Injectable Conductive Hydrogels for Tissue Engineering Application. *Tissue Eng., Part B* **2019**, *25*, 398.
- (7) Eswaramoorthy, S. D.; Ramakrishna, S.; Rath, S. N. Recent advances in three-dimensional bioprinting of stem cells. *J. Tissue Eng. Regen. Med.* **2019**, *13*, 908.
- (8) Dehli, F.; Rebers, L.; Stubenrauch, C.; Southan, A. Highly ordered gelatin methacryloyl hydrogel foams with tunable pore size. *Biomacromolecules* **2019**, *20*, 2666.
- (9) Sionkowska, A. Current research on the blends of natural and synthetic polymers as new biomaterials: Review. *Prog. Polym. Sci.* **2011**, *36*, 1254–1276.
- (10) O'Brien, F. J. Biomaterials & scaffolds for tissue engineering. *Mater. Today* **2011**, *14*, 88–95.
- (11) Armiento, A. R.; Stoddart, M. J.; Alini, M.; Eglin, D. Biomaterials for articular cartilage tissue engineering: Learning from biology. *Acta Biomater.* **2018**, *65*, 1–20.
- (12) Qasim, M.; Chae, D. S.; Lee, N. Y. Advancements and frontiers in nano-based 3D and 4D scaffolds for bone and cartilage tissue engineering. *Int. J. Nanomed.* **2019**, *14*, 4333–4351.
- (13) Vroman, I.; Tighzert, L. Biodegradable Polymers. *Materials* **2009**, *2*, 307.
- (14) Leach, D. G.; Young, S.; Hartgerink, J. D. Advances in immunotherapy delivery from implantable and injectable biomaterials. *Acta Biomater.* **2019**, *88*, 15–31.
- (15) Trucco, D.; Vannozzi, L.; Teblum, E.; Telkhozhayeva, M.; Nessim, G. D.; Affatato, S.; Al-Haddad, H.; Lisignoli, G.; Ricotti, L. Graphene Oxide-Doped Gellan Gum-PEGDA Bilayered Hydrogel Mimicking the Mechanical and Lubrication Properties of Articular Cartilage. *Adv. Healthcare Mater.* **2021**, *10*, 2001434.
- (16) Loh, Q. L.; Choong, C. Three-dimensional scaffolds for tissue engineering applications: role of porosity and pore size. *Tissue Eng., Part B* **2013**, *19*, 485–502.
- (17) Li, M. G.; Tian, X. Y.; Chen, X. B. A brief review of dispensing-based rapid prototyping techniques in tissue scaffold fabrication: role of modeling on scaffold properties prediction. *Biofabrication* **2009**, *1*, 032001.
- (18) Li, J.; Chen, G.; Xu, X.; Abdou, P.; Jiang, Q.; Shi, D.; Gu, Z. Advances of injectable hydrogel-based scaffolds for cartilage regeneration. *Regener. Biomater.* **2019**, *6*, 129–140.
- (19) Ng, W. L.; Lee, J. M.; Zhou, M.; Chen, Y.-W.; Lee, K.-X. A.; Yeong, W. Y.; Shen, Y.-F. Vat polymerization-based bioprinting—process, materials, applications and regulatory challenges. *Biofabrication* **2020**, *12*, 022001.

- (20) Hölzl, K.; Lin, S.; Tytgat, L.; Van Vlierberghe, S.; Gu, L.; Ovsianikov, A. Bioink properties before, during and after 3D bioprinting. *Biofabrication* **2016**, *8*, 032002.
- (21) Paxton, N.; Smolan, W.; Böck, T.; Melchels, F.; Groll, J.; Jungst, T. Proposal to assess printability of bioinks for extrusion-based bioprinting and evaluation of rheological properties governing bioprintability. *Biofabrication* **2017**, *9*, 044107.
- (22) Emmermacher, J.; Spura, D.; Cziommer, J.; Kilian, D.; Wollborn, T.; Fritsching, U.; Steingroewer, J.; Walther, T.; Gelinsky, M.; Lode, A. Engineering considerations on extrusion-based bioprinting: interactions of material behavior, mechanical forces and cells in the printing needle. *Biofabrication* **2020**, *12*, 025022.
- (23) Zhao, Y.; Li, Y.; Mao, S.; Sun, W.; Yao, R. The influence of printing parameters on cell survival rate and printability in microextrusion-based 3D cell printing technology. *Biofabrication* **2015**, *7*, 045002.
- (24) Suntornond, R.; Tan, E.; An, J.; Chua, C. A Mathematical Model on the Resolution of Extrusion Bioprinting for the Development of New Bioinks. *Materials* **2016**, *9*, 756.
- (25) Chawla, S.; Kumar, A.; Admane, P.; Bandyopadhyay, A.; Ghosh, S. Elucidating role of silk-gelatin bioink to recapitulate articular cartilage differentiation in 3D bioprinted constructs. *Bioprinting* **2017**, *7*, 1–13.
- (26) Chawla, S.; Sharma, A.; Bandyopadhyay, A.; Ghosh, S. Developmental Biology-Inspired Strategies To Engineer 3D Bioprinted Bone Construct. *ACS Biomater. Sci. Eng.* **2018**, *4*, 3545–3560.
- (27) Midha, S.; Murab, S.; Ghosh, S. Osteogenic signaling on silk-based matrices. *Biomaterials* **2016**, *97*, 133–153.
- (28) Dubey, P.; Murab, S.; Karmakar, S.; Chowdhury, P. K.; Ghosh, S. Modulation of Self-Assembly Process of Fibroin: An Insight for Regulating the Conformation of Silk Biomaterials. *Biomacromolecules* **2015**, *16*, 3936–3944.
- (29) Kasoju, N.; Bora, U. Silk Fibroin in Tissue Engineering. *Adv. Healthcare Mater.* **2012**, *1*, 393–412.
- (30) Rockwood, D. N.; Preda, R. C.; Yücel, T.; Wang, X.; Lovett, M. L.; Kaplan, D. L. Materials Fabrication from Bombyx mori Silk Fibroin. *Nat. Protoc.* **2011**, *6*, 1612.
- (31) Ghosh, S.; Parker, S. T.; Wang, X.; Kaplan, D. L.; Lewis, J. A. Direct-Write Assembly of Microperiodic Silk Fibroin Scaffolds for Tissue Engineering Applications. *Adv. Funct. Mater.* **2008**, *18*, 1883–1889.
- (32) Nisal, A.; Kalelkar, C.; Bellare, J.; Lele, A. Rheology and microstructural studies of regenerated silk fibroin solutions. *Rheol. Acta* **2013**, *52*, 833–840.
- (33) Laity, P. R.; Gilks, S. E.; Holland, C. Rheological behaviour of native silk feedstocks. *Polymer* **2015**, *67*, 28–39.
- (34) Das, S.; Pati, F.; Chameettachal, S.; Pahwa, S.; Ray, A. R.; Dhara, S.; Ghosh, S. Enhanced Redifferentiation of Chondrocytes on Microperiodic Silk/Gelatin Scaffolds: Toward Tailor-Made Tissue Engineering. *Biomacromolecules* **2013**, *14*, 311.
- (35) Xiao, W.; Li, J.; Qu, X.; Wang, L.; Tan, Y.; Li, K.; Li, H.; Yue, X.; Li, B.; Liao, X. Cell-laden interpenetrating network hydrogels formed from methacrylated gelatin and silk fibroin via a combination of sonication and photocrosslinking approaches. *Mater. Sci. Eng., C* **2019**, *99*, 57–67.
- (36) Chawla, S.; Midha, S.; Sharma, A.; Ghosh, S. Silk-Based Bioinks for 3D Bioprinting. *Adv. Healthcare Mater.* **2018**, *7*, 1701204.
- (37) Hsia, H. C.; Nair, M. R.; Mintz, R. C.; Corbett, S. A. The fiber diameter of synthetic bioresorbable extracellular matrix influences human fibroblast morphology and fibronectin matrix assembly. *Plast. Reconstr. Surg.* **2011**, *127*, 2312–2320.
- (38) Sharma, A.; Desando, G.; Petretta, M.; Chawla, S.; Bartolotti, I.; Manferdini, C.; Paoletta, F.; Gabusi, E.; Trucco, D.; Ghosh, S.; Lisignoli, G. Investigating the Role of Sustained Calcium Release in Silk-Gelatin-Based Three-Dimensional Bioprinted Constructs for Enhancing the Osteogenic Differentiation of Human Bone Marrow Derived Mesenchymal Stromal Cells. *ACS Biomater. Sci. Eng.* **2019**, *5*, 1518.
- (39) Jiang, T.; Munguia-Lopez, J.; Flores-Torres, S.; Grant, J.; Vijayakumar, S.; De Leon-Rodriguez, A.; Kinsella, J. M. Bioprintable Alginate/Gelatin Hydrogel 3D In Vitro Model Systems Induce Cell Spheroid Formation. *J. Visualized Exp.* **2018**, *137*, 57826.
- (40) Simpson, M. M.; Janna, W. S. Newtonian and Non-Newtonian Fluids: Velocity Profiles, Viscosity Data, and Laminar Flow Friction Factor Equations for Flow in a Circular Duct. *ASME 2008 International Mechanical Engineering Congress and Exposition*, 2008; pp 173–180.
- (41) Blaeser, A.; Duarte Campos, D. F.; Puster, U.; Richtering, W.; Stevens, M. M.; Fischer, H. Controlling Shear Stress in 3D Bioprinting is a Key Factor to Balance Printing Resolution and Stem Cell Integrity. *Adv. Healthcare Mater.* **2016**, *5*, 326–333.
- (42) Lee, J. M.; Yeong, W. Y. A preliminary model of time-pressure dispensing system for bioprinting based on printing and material parameters. *Virtual Phys. Prototyp.* **2015**, *10*, 3–8.
- (43) Agrawal, C. M.; McKinney, J. S.; Lanctot, D.; Athanasiou, K. A. Effects of fluid flow on the in vitro degradation kinetics of biodegradable scaffolds for tissue engineering. *Biomaterials* **2000**, *21*, 2443–2452.
- (44) Yang, J.; Li, Y.; Liu, Y.; Li, D.; Zhang, L.; Wang, Q.; Xiao, Y.; Zhang, X. Influence of hydrogel network microstructures on mesenchymal stem cell chondrogenesis in vitro and in vivo. *Acta Biomater.* **2019**, *91*, 159–172.
- (45) Lisignoli, G.; Cristino, S.; Piacentini, A.; Toneguzzi, S.; Grassi, F.; Cavallo, C.; Zini, N.; Solimando, L.; Mario Maraldi, N.; Facchini, A. Cellular and molecular events during chondrogenesis of human mesenchymal stromal cells grown in a three-dimensional hyaluronan based scaffold. *Biomaterials* **2005**, *26*, 5677–5686.
- (46) Das, S.; Pati, F.; Choi, Y.-J.; Rijal, G.; Shim, J.-H.; Kim, S. W.; Ray, A. R.; Cho, D.-W.; Ghosh, S. Bioprintable, cell-laden silk fibroin-gelatin hydrogel supporting multilineage differentiation of stem cells for fabrication of three-dimensional tissue constructs. *Acta Biomater.* **2015**, *11*, 233–246.
- (47) Chen, X. B. Modeling and control of fluid dispensing processes: a state-of-the-art review. *Int. J. Adv. Manuf. Technol.* **2009**, *43*, 276–286.
- (48) Spoerk, M.; Gonzalez-Gutierrez, J.; Sapkota, J.; Schuschnigg, S.; Holzer, C. Effect of the printing bed temperature on the adhesion of parts produced by fused filament fabrication. *Plast., Rubber Compos.* **2018**, *47*, 17–24.
- (49) Li, M. G.; Tian, X. Y.; Chen, X. B. Modeling of Flow Rate, Pore Size, and Porosity for the Dispensing-Based Tissue Scaffolds Fabrication. *J. Manuf. Sci. Eng.* **2009**, *131*, 034501.
- (50) Sultan, S.; Mathew, A. P. 3D printed scaffolds with gradient porosity based on a cellulose nanocrystal hydrogel. *Nanoscale* **2018**, *10*, 4421–4431.
- (51) Park, H.; Guo, X.; Temenoff, J. S.; Tabata, Y.; Caplan, A. I.; Kasper, F. K.; Mikos, A. G. Effect of Swelling Ratio of Injectable Hydrogel Composites on Chondrogenic Differentiation of Encapsulated Rabbit Marrow Mesenchymal Stem Cells In Vitro. *Biomacromolecules* **2009**, *10*, 541–546.
- (52) Naleway, S. E.; Porter, M. M.; McKittrick, J.; Meyers, M. A. Structural Design Elements in Biological Materials: Application to Bioinspiration. *Adv. Mater.* **2015**, *27*, 5455–5476.
- (53) Slaughter, B. V.; Khurshid, S. S.; Fisher, O. Z.; Khademhosseini, A.; Peppas, N. A. Hydrogels in Regenerative Medicine. *Adv. Mater.* **2009**, *21*, 3307–3329.
- (54) Caccavo, D.; Cascone, S.; Lamberti, G.; Barba, A. A. Hydrogels: experimental characterization and mathematical modelling of their mechanical and diffusive behaviour. *Chem. Soc. Rev.* **2018**, *47*, 2357–2373.
- (55) Kim, T.; Kim, M.-S.; Goh, T. S.; Lee, J. S.; Kim, Y. H.; Yoon, S.-Y.; Lee, C.-S. Evaluation of Structural and Mechanical Properties of Porous Artificial Bone Scaffolds Fabricated via Advanced TBA-Based Freeze-Gel Casting Technique. *Appl. Sci.* **2019**, *9*, 1965.
- (56) Billiet, T.; Gevaert, E.; De Schryver, T.; Cornelissen, M.; Dubrue, P. The 3D printing of gelatin methacrylamide cell-laden

tissue-engineered constructs with high cell viability. *Biomaterials* **2014**, *35*, 49–62.

(57) Li, M.; Tian, X.; Kozinski, J. A.; Chen, X.; Hwang, D. K. MODELING MECHANICAL CELL DAMAGE IN THE BIOPRINTING PROCESS EMPLOYING A CONICAL NEEDLE. *J. Mech. Med. Biol.* **2015**, *15*, 1550073.

(58) Li, M.; Tian, X.; Schreyer, D. J.; Chen, X. Effect of needle geometry on flow rate and cell damage in the dispensing-based biofabrication process. *Biotechnol. Prog.* **2011**, *27*, 1777–1784.

(59) Camarero-Espinosa, S.; Rothen-Rutishauser, B.; Foster, E. J.; Weder, C. Articular cartilage: from formation to tissue engineering. *Biomater. Sci.* **2016**, *4*, 734–767.

(60) Carballo, C. B.; Nakagawa, Y.; Sekiya, I.; Rodeo, S. A. Basic Science of Articular Cartilage. *Clin. Sports Med.* **2017**, *36*, 413–425.

(61) Ng, H. Y.; Shen, Y.-F. Articular Cartilage: Structure, Composition, Injuries and Repair. *JSM Bone Jt. Dis.* **2017**, *1*, 1010.

(62) Chakraborty, J.; Ghosh, S. Cellular Proliferation, Self-Assembly, and Modulation of Signaling Pathways in Silk Fibroin Gelatin-Based 3D Bioprinted Constructs. *ACS Appl. Bio Mater.* **2020**, *3*, 8309–8320.

(63) Melke, J.; Midha, S.; Ghosh, S.; Ito, K.; Hofmann, S. Silk fibroin as biomaterial for bone tissue engineering. *Acta Biomater.* **2016**, *31*, 1–16.

(64) Zheng, Z.; Wu, J.; Liu, M.; Wang, H.; Li, C.; Rodriguez, M. J.; Li, G.; Wang, X.; Kaplan, D. L. 3D Bioprinting of Self-Standing Silk-Based Bioink. *Adv. Healthcare Mater.* **2018**, *7*, 1701026.

(65) Li, X.; Sun, Q.; Li, Q.; Kawazoe, N.; Chen, G. Functional Hydrogels With Tunable Structures and Properties for Tissue Engineering Applications. *Front. Chem.* **2018**, *6*, 499.

(66) Lou, J.; Stowers, R.; Nam, S.; Xia, Y.; Chaudhuri, O. Stress relaxing hyaluronic acid-collagen hydrogels promote cell spreading, fiber remodeling, and focal adhesion formation in 3D cell culture. *Biomaterials* **2018**, *154*, 213–222.

(67) Wang, L.-S.; Du, C.; Toh, W. S.; Wan, A. C. A.; Gao, S. J.; Kurisawa, M. Modulation of chondrocyte functions and stiffness-dependent cartilage repair using an injectable enzymatically cross-linked hydrogel with tunable mechanical properties. *Biomaterials* **2014**, *35*, 2207–2217.

(68) Li, X.; Chen, S.; Li, J.; Wang, X.; Zhang, J.; Kawazoe, N.; Chen, G. 3D Culture of Chondrocytes in Gelatin Hydrogels with Different Stiffness. *Polymers* **2016**, *8*, 269.

(69) Chawla, S.; Desando, G.; Gabusi, E.; et al. The effect of silk-gelatin bioink and TGF- β 3 on mesenchymal stromal cells in 3D bioprinted chondrogenic constructs: a proteomic study. *J. Mater. Res.* **2021**, DOI: 10.1557/s43578-021-00230-5.